PHYSICAL REVIEW MATERIALS **2**, 085003 (2018)

Crystal growth and metal-insulator transition in two-dimensional layered rare-earth palladates

Yoshiko Nanao,[1,2,*] Yoshiharu Krockenberger,[1] Ai Ikeda,[1] Yoshitaka Taniyasu,[1] Michio Naito,[2] and Hideki Yamamoto[1]
[1]*NTT Basic Research Laboratories, NTT Corporation, 3-1 Morinosato-Wakamiya, Atsugi, Kanagawa 243-0198, Japan*
[2]*Department of Applied Physics, Tokyo University of Agriculture and Technology TUAT, 2-24-16 Nakamachi, Koganei, Tokyo 184-8588, Japan*

(Received 31 May 2018; published 15 August 2018)

We synthesized high-quality, single-crystalline thin films of layered rare-earth (R) palladates R_2PdO_4 ($R =$ La, Nd, and Sm) and Ce substituted $Nd_{2-x}Ce_xPdO_4$ by reactive molecular beam epitaxy. For La_2PdO_4, Nd_2PdO_4, and Sm_2PdO_4, we find that the electronic conduction is independent of R elements. Doping charge carriers into the PdO_2 planes of $Nd_{2-x}Ce_xPdO_4$ increases the electronic conduction and this effect is enhanced by vacuum annealing. The enhanced electronic conduction originates not solely from the doped charge carriers but is superimposed by Pd vacancies. X-ray photoelectron spectroscopy combined with inductively coupled plasma mass spectrometry revealed Pd deficiencies in $Nd_{2-x}Ce_xPdO_4$ and these defects play a crucial role for the electronic conduction. We observe a monotonic enhancement of the electronic conduction in $Nd_{2-x}Ce_xPdO_4$ thin films induced by Ce substitution and vacuum annealing. The estimated charge carrier concentration necessary for metallic conduction ($x \approx 0.45$) at $T = 0$ K is far beyond the experimentally accessible solubility limit.

DOI: 10.1103/PhysRevMaterials.2.085003

I. INTRODUCTION

The 4d transition-metal oxides are known for their variety of electronic properties. For example, the ruthenate family $Sr_{n+1}Ru_nO_{3n+1}$ (n: positive integer, Ruddlesden-Popper series) is known to generate a ferromagnetic metal $SrRuO_3$ ($n = \infty$) [1] as well as a superconductor Sr_2RuO_4 ($n = 1$) [2,3]. Metallic conduction is also observed in neighboring 4d Ruddlesden-Popper compounds, e.g., $Sr_{n+1}Mo_nO_{3n+1}$ [4] and $Sr_{n+1}Rh_nO_{3n+1}$ [5]. This raises the question of the electronic conduction in palladates. While $LaPdO_3$ [6] has been synthesized and found to crystallize in an orthorhombic unit cell (*Pbnm*), its electronic conduction remains unknown. This is also the case for layered $R_{n+1}Pd_nO_{3n+1}$, with $n = 1$, where PdO_2 planes form an infinite two-dimensional network. Quite generally, the electronic conduction in palladates is ruled by the Pd-Pd distance ($d_{\mathrm{Pd-Pd}}$), and this is in contrast to other 4d transition-metal oxides. We visualized this trend in Fig. 1 where the resistivity values at 300 K are plotted as a function of the $d_{\mathrm{Pd-Pd}}$ for various palladates. Data are taken from references listed in Table I. It is remarkable that the range of the resistivity varies over 18 orders of magnitude. Particularly for $PdCoO_2$, Mackenzie [7] reported that it has one of the lowest electrical resistivities (~2.6 $\mu\Omega$cm) among all oxides. Meanwhile, very high resistivity values have been reported for La_4PdO_7 [8], which has the largest $d_{\mathrm{Pd-Pd}}$ distance (Fig. 1). In addition to the Pd-Pd hybridization, charge carrier doping can induce metallic conduction into intrinsically insulating palladates. For example, the binary palladium oxide PdO, which consists of two perpendicularly overlapping PdO chains, is a p-type semiconductor and it may be rendered into a metallic state by as little as 1 % Li substitution [9]. The fact that the electronic conduction increases by decreasing the $d_{\mathrm{Pd-Pd}}$ (Fig. 1) holds for almost all palladates, but R_2PdO_4. Despite having nearly the same $d_{\mathrm{Pd-Pd}}$ distance as R_4PdO_7 [10], the electronic conduction for R_2PdO_4 is enhanced by 12 orders of magnitude. This enhancement supposedly stems from the ordering and rearrangement of disconnected PdO_2 plaquettes found in R_4PdO_7 towards two-dimensional, corner-sharing PdO_2 planes (Fig. 2).

Commonly, Pd^{2+} ions stabilize a square-planar coordination in their oxides [48,49], and this is exceptional compared to other 4d Ruddlesden-Popper oxides (for example, $Sr_{n+1}Rh_nO_{3n+1}$ has RhO_6 octahedrons). Comparing R_2PdO_4 to other 4d Ruddlesden-Popper oxides, R_2PdO_4 has the highest valence electron number causing additional complications. A system with the same electron count as Nd_2PdO_4 is La_2NiO_4. Such layered nickelates have been investigated by photoemission spectroscopy [50] and found to be charge-transfer (CT) insulators with a CT gap of ~4 eV. Moreover, the authors found that this gap value is unaltered when compared to NiO [51]. The doped holes in $La_{2-x}Sr_xNiO_4$ occupy empty states above the Fermi level, which results in a metal-insulator transition at a doping concentration as high as $x \approx 0.8$ [52]. Having the same electron configuration as nickelates, one might expect a similar scenario for palladates. Rather than the NiO_6 octahedrons found in La_2NiO_4, Pd forms square plaquettes, thus stabilizing a different coordination. Moreover, Pd is a 4d element and, has a significant higher mass ($Z = 46$) than Ni ($Z = 28$), and the spin-orbit-coupling (SOC) contribution to the electronic ground-state energy can no longer be ignored [53,54]. The enhanced SOC causes a significant broadening of the electronic states, which is visualized in Fig. 3 [55]. While the energy gap for La_2NiO_4 is 4 eV, the band gap for R_2PdO_4 is unknown. Nonetheless, the optical band gap of PdO has been reported to be ~0.8–2.0 eV [56–65]. For Ba_2PdO_3 and La_4PdO_7, both crystal structures with square-planar coordinated Pd^{2+} ions and band structure calculations [66] suggest that their electronic structure is not significantly different from the widely

---

[*] y05hik0nana0@gmail.com

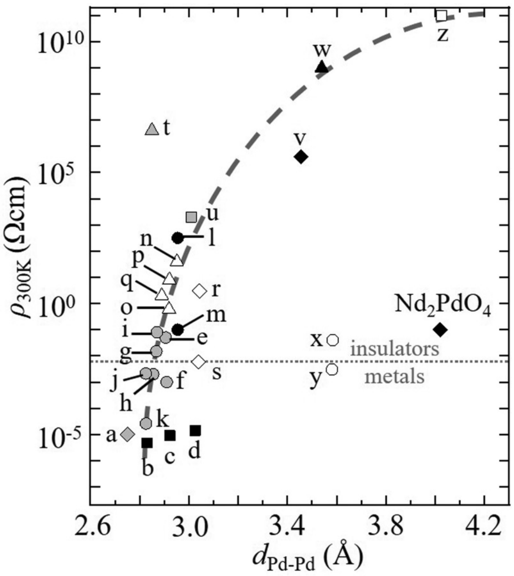

FIG. 1. Relationship between electronic conduction and Pd-Pd distance in palladates and a metal Pd. Details are listed in Table I. The dashed line is a guide to the eye. Nd_2PdO_4 does not follow this trend, suggesting that electron correlations are more important than Pd-Pd hybridization. The dotted line represents the threshold between insulating and metallic palladates.

studied PdO. Therefore, we assume that a similar scenario holds for palladates and a band-gap value for Nd_2PdO_4 to be ∼0.8–2.0 eV (see Fig. 3). While the scenario of the electronic states of the undoped Nd_2PdO_4 is somewhat resembled by that of the undoped La_2NiO_4, the development of the electronic density of states for hole-doped $La_{2-x}Sr_xNiO_4$ and electron-doped $Nd_{2-x}Ce_xPdO_4$ is entirely different. In contrast to the hole-doped La_2NiO_4 system, the Fermi level is expected to shift relatively toward the d^9 band for the electron-doped R_2PdO_4 system. Based on this scenario, we doped electrons via Ce^{4+} substitution in Nd_2PdO_4 to enhance the electronic conductivity towards a metallic state. The question still remains to be solved as to how many charge carriers are necessary to fill the band gap or occupy empty states at the Fermi energy in R_2PdO_4, and whether the doping concentration will conflict with the solubility limit at the critical doping concentration.

In this paper, we focus our attention on the synthesis of Nd_2PdO_4, La_2PdO_4, and Sm_2PdO_4 thin films along with electron doping by Ce into Nd_2PdO_4. To ensure that the crystal quality of our palladate films suffices for the requirements set to electronic materials, we use molecular beam epitaxy (MBE) for their synthesis. While the synthesis and electronic conduction for sintered samples of $Nd_{2-x}Ce_xPdO_4$ were reported previously [67–69], the intrinsic electronic conduction is hampered by the existence of grain boundaries. Tracing the

TABLE I. A list of palladates and their associated d_{Pd-Pd} (Å), $\rho_{300\,K}$ (Ωcm), and space groups used for Fig. 1. For $LaPdO_3$ [6], R_2BaPdO_5 [40–42], KPd_2O_3 [43], $K_3Pd_2O_4$ [27], $Ba_2Hg_3Pd_7O_{14}$ [45], $Na_2Pd_3O_4$ [44], $(Sr,Ca)_4PdO_6$ [46], and Zn_2PdO_4 [47], resistivity values are not available.

Label	Material	d_{Pd-Pd} (Å)	$\rho_{300\,K}$ (Ωcm)	Space group	References
a	Pd	2.75	1.03×10^{-5}	$Fm\bar{3}m$	[11–15]
b	$PdCoO_2$	2.830	2.6×10^{-6}	$R\bar{3}m$	[7,16,17]
c	$PdCrO_2$	2.923	9.0×10^{-6}	$R\bar{3}m$	[18,19]
d	$PdRhO_2$	3.025	1.4×10^{-5}	$R\bar{3}m$	[20,21]
e	$SrPd_3O_4$	2.906	0.05	$Pm\bar{3}n$	[22–24]
f	$Sr_{0.8}Na_{0.2}Pd_3O_4$	2.910	1.0×10^{-3}	$Pm\bar{3}n$	[22,24]
g	$CaPd_3O_4$	2.868	0.015	$Pm\bar{3}n$	[23,25]
h	$Ca_{0.6}Li_{0.4}Pd_3O_4$	2.855	2.0×10^{-3}	$Pm\bar{3}n$	[26]
i	$Ca_{0.53}Na_{0.47}Pd_3O_4$	2.870	0.08	$Pm\bar{3}n$	[25]
j	$NaPd_3O_4$	2.825	2.1×10^{-3}	$Pm\bar{3}n$	[25,27]
k	$Gd_xPd_3O_4$	2.826	2.6×10^{-5}	$Pm\bar{3}n$	[28]
l	Bi_2PdO_4	2.955	316	$I4cm$	[29]
m	$Bi_{1.925}Pb_{0.075}PdO_4$	2.955	0.1	$I4cm$	[30]
n	$LaPd_2O_4$	2.951	40	$I4_1/a$	[31,32]
o	$PrPd_2O_4$	2.919	0.6	$I4_1/a$	[32]
p	$NdPd_2O_4$	2.921	8.0	$I4_1/a$	[32]
q	$GdPd_2O_4$	2.890	2.0	$I4_1/a$	[32]
r	PdO	3.043	3.0	$P4_2/mmc$	[9]
s	$Pd_{0.7}Li_{0.3}O$	3.039	6.0×10^{-3}	$P4_2/mmc$	[9]
t	$La_2Pd_2O_5$	2.850	4.0×10^6	$P4_2/mmc$	[8]
u	Ag_2PdO_2	3.009	2.0×10^3	$P4_2/mmc$	[33]
v	$LiBiPd_2O_4$	3.455	4.0×10^5	$P4/nmm$	[34,35]
w	Sr_2PdO_3	3.539	1.0×10^9	$Immm$	[36,37]
x	$PbPdO_2$	3.583	4.0×10^{-2}	$Imma$	[38]
y	$PbLi_{0.08}Pd_{0.92}O_2$	3.581	3.0×10^{-3}	$Imma$	[38]
z	La_4PdO_7	4.026	$>1.0 \times 10^{11}$	$C2/m$	[8]
Nd_2PdO_4	Nd_2PdO_4	4.02	1.0×10^{-1}	$I4/mmm$	[39]

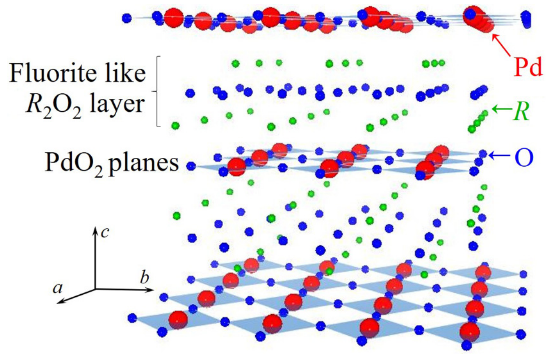

FIG. 2. The crystal structure of R_2PdO_4 ($I4/mmm$, No. 139). PdO_2 planes are stacked along the c axis and sandwiched between R_2O_2 layers. Pd^{2+} ions are square coordinated. This structure is called the T' structure.

electronic conduction variation induced by doping demands single-crystalline samples over a wide doping range.

II. EXPERIMENTAL DETAILS

The phase formation of the layered palladates, namely, R_2PdO_4, is thermodynamically competing with other palladates, e.g., R_4PdO_7 and $R_2Pd_2O_5$ [39]. It is fortunate that the presence of rare-earth ions act as a stabilizer for Pd^{2+} ions, and therefore allow for synthesis conditions beyond the decomposition temperature of PdO. However, it is essential to simultaneously control both the stoichiometry (atomic beam flux ratios) and thermodynamics [synthesis temperature (T_s) and flux of atomic oxygen] for the synthesis of layered palladates. To optimize the growth conditions with respect to the crystal quality, we varied T_s from 600 to 925 °C by 25 °C steps in a customer-designed MBE chamber equipped with 10 electron gun sources. The T_s required for the formation of La_2PdO_4, Nd_2PdO_4, and Sm_2PdO_4 are nearly identical to each other and therefore independent of the R ions. Also, for Ce-doped palladates ($Nd_{2-x}Ce_xPdO_4$), T_s is close to that of undoped Nd_2PdO_4. We find the optimal growth temperature to be $T_s = 850 \pm 20\,^{\circ}C$. Owing to the slow oxidizing kinetics of Pd, the thermodynamic window for the synthesis of T' palladates is dominated by the oxidization kinetics of Pd.

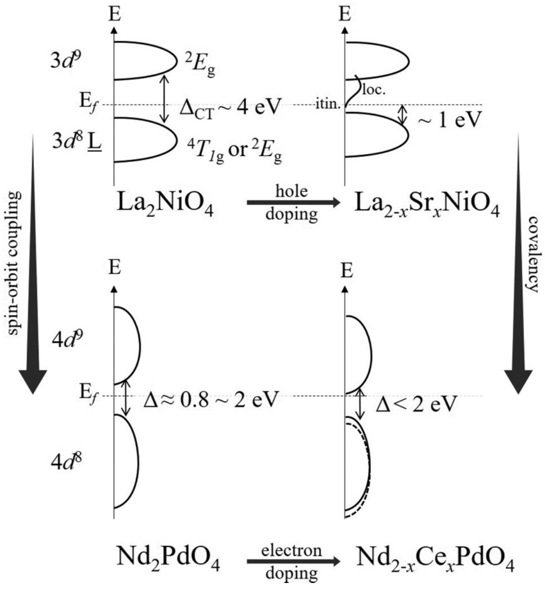

FIG. 3. Schematic electronic diagrams of hole-doped $La_{2-x}Sr_xNiO_4$ and electron-doped $Nd_{2-x}Ce_xPdO_4$. For undoped La_2NiO_4, the charge-transfer (CT) gap is ∼4 eV and the doped holes occupy empty states above the Fermi level. The positions of itinerant and localized holes are labeled by itin. and loc., respectively. For Nd_2PdO_4, the electronic band gap is expected to be 0.8–2.0 eV and we confirmed the upper limit by EELS measurements. For Nd_2PdO_4, the density of states are smeared out over a wider range due to the 4d states and the enhanced spin-orbit coupling. The doped electrons lift the Fermi level.

The oxidation of oxophobic transition metals is a challenge, particularly under ultrahigh vacuum conditions. Atomic oxygen is a powerful species as it minimizes the energy barrier of the oxidizing process of elemental Pd. We varied the radio-frequency power of the atomic oxygen source as well as the oxygen flow rate in the range of 150 to 400 W and 0.25 to 4.50 sccm, respectively, and this led to optimal oxidizing conditions at 250–300 W with an oxygen flow of 1.20–1.50 sccm. The atomic beam flux of each constituent element was controlled by electron impact emission spectroscopy (EIES) [70]. At optimal growth temperature and oxidizing conditions, the deposition rates for La, Nd, and Sm are fixed at 1.26, 1.15, and 1.12 Å/s, respectively. The deposition rate of Pd was varied between 0.53 and 0.66 Å/s, resulting in a growth rate of R_2PdO_4 of approximately 0.1 layers/s [71]. The typical film thickness of each growth is 80 or 160 nm, subject to the deposition time. Owing to the weak electronic emission characteristic of elemental Ce, EIES is an unsuitable technique for the control of the Ce flux, and therefore a quartz-crystal microbalance (QCM) was used instead. The Ce concentration x used here ranges from 0 to 0.3 corresponding to Nd and Ce fluxes between 1.15 to 0.98 Å/s and 0 to 0.17 Å/s, respectively, in $Nd_{2-x}Ce_xPdO_4$. All of the films discussed here are grown on (001) $SrTiO_3$ substrates. For complex transition-metal oxides, it is well known that annealing treatments are beneficial to the crystal quality of the grown material. Here, we adopted an *in situ* vacuum annealing process for 10 min. During the vacuum annealing process, the chamber pressure was kept at $\sim 10^{-9}$ Torr. X-ray diffraction measurements were done using monochromatic Cu K_{α_1} radiation in a Bruker D8 four-circle diffractometer. Resistivity values were determined using a standard four-probe method with Ag electrodes in a liquid He dewar. Additional electronic transport measurements were carried out between 400 and 1.8 K in a Quantum Design DynaCool PPMS. The cation ratios were independently determined by inductively coupled plasma (ICP) analysis. Electron energy loss spectroscopy (EELS) measurements for the determination of the optical band gap of Nd_2PdO_4 films were carried out using an aberration-corrected scanning transmission electron microscope JEOL JEM ARM 200F. X-ray photoemission spectroscopy (XPS) data were collected in a PHI 5700 spectrometer equipped with a twin anode delivering Al K_α and Mg K_α radiations (1486.6 and 1253.6 eV, respectively). With the monochromatic Al K_α source, the energy resolution for XPS is 0.4 eV. The examined materials and experimental conditions are summarized in Table II.

TABLE II. A list of $R_{2-x}Ce_xPdO_4$ films together with thickness, synthesis temperature (T_s), and annealing procedure. For all films, (001) $SrTiO_3$ was used as the substrate material. The annealing process was performed *in situ*.

Film no.	Composition	Thickness (nm)	T_s (°C)	Annealing process
A	La_2PdO_4	80	846	as-grown
B	Nd_2PdO_4	160	846	as-grown
C	Nd_2PdO_4	160	846	as-grown
D	Nd_2PdO_4	80	846	771 °C in vacuum
E	Nd_2PdO_4	160	846	765 °C in vacuum
F	Sm_2PdO_4	80	833	as-grown
G	$Nd_{1.93}Ce_{0.07}PdO_4$	80	846	as-grown
H	$Nd_{1.93}Ce_{0.07}PdO_4$	80	846	765 °C in vacuum
I	$Nd_{1.81}Ce_{0.19}PdO_4$	80	856	719 °C in vacuum
J	$Nd_{1.81}Ce_{0.19}PdO_4$	160	856	719 °C in vacuum
K	$Nd_{1.81}Ce_{0.19}PdO_4$	160	856	719 °C in vacuum
L	$Nd_{1.81}Ce_{0.19}PdO_4$	160	856	719 °C in vacuum
M	$Nd_{1.81}Ce_{0.19}PdO_4$	160	856	765 °C in vacuum
N	$Nd_{1.76}Ce_{0.24}PdO_4$	160	833	as-grown
O	$Nd_{1.76}Ce_{0.24}PdO_4$	160	833	719 °C in vacuum
P	$Nd_{1.76}Ce_{0.24}PdO_4$	160	856	719 °C in vacuum
Q	$Nd_{1.71}Ce_{0.29}PdO_4$	160	852	716 °C in vacuum

III. SOLUBILITY LIMIT ESTIMATION

The phase stability of Nd_2PdO_4 and $Nd_{2-x}Ce_xPdO_4$ depends not only on the thermodynamic conditions during their synthesis, but also on the local crystal geometry. As a well-known example, the high-temperature superconductors R_2CuO_4 are known to crystallize in three different phases, where the Cu^{2+} ions are either square-planar, pyramidal, or octahedral coordinated, and the different phases are driven by the dimensions of the R ions. Mixing different R ions in $R_{2-x}R'_xCuO_4$ allows for a maximum concentration of R' for a given coordination geometry $x_{\max}$, and this is called the solubility limit of R' in $R_{2-x}R'_xCuO_4$. For Nd_2CuO_4, a cuprate which has the same crystal structure as the layered palladates discussed here, the solubility limit of Ce is about 0.18 ($Nd_{1.82}Ce_{0.18}CuO_4$) [72], and higher Ce concentrations result in a different coordination geometry of copper. For $R_{2-x}Ce_xPdO_4$, Pd^{2+} ions are also square-planar coordinated and despite their larger ionic radius (0.64 Å), the crystal structure is the same as for Nd_2CuO_4 (ionic radius of Cu^{2+} is 0.57 Å). For the purpose of determining the solubility limit of Ce in $Nd_{2-x}Ce_xPdO_4$, we use a simple geometrical abstraction of the ions involved (Fig. 4). Here, $r^{\mathrm{CN}}_{\mathrm{ion}^{\mathrm{VN}}}$ represents the ionic radii given by Shannon [73] (VN is the valency and CN the coordination number) and we regard the ions of $Nd_{2-x}Ce_xPdO_4$ as hard spheres. When we substitute x% of R ions with Ce ions, the average ionic radius can be written as

$$r_{\mathrm{avg}} = (1-x) \times r_{R^{3+}} + x \times r_{\mathrm{Ce}^{4+}}. \qquad (1)$$

To visualize the geometric arrangement of cations and oxygen ions of the $Nd_{2-x}Ce_xPdO_4$ phase, we draw the fluorite layer of Nd_2PdO_4 in Fig. 4.

The smallest possible RO_8 cube is achieved when the center R ion is coordinated by eight O^{2-} ions at the corners of the cube, and the O^{2-} ions are touching each other. Under such conditions, the largest possible ionic radius of R ions is $r^{\mathrm{VIII}}_{R^{3+}\max} = (\sqrt{3}-1) \times r^{\mathrm{IV}}_{\mathrm{O}^{2-}}$. With $r^{\mathrm{IV}}_{\mathrm{O}^{2-}} = 1.38$ Å [73], the maximum radius of the rare-earth ion at the center of the cube becomes $r_{R^{3+}\max} = 1.01$ Å.

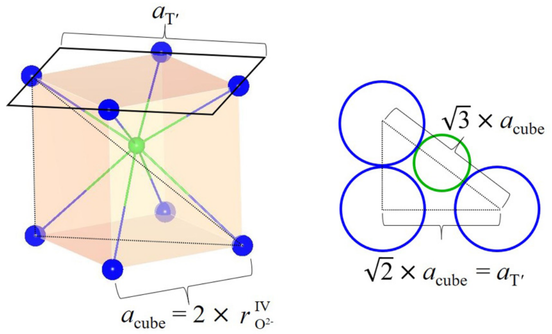

FIG. 4. Sketch of the RO_8 cube of Nd_2PdO_4 (left) and its vicinal cut plane (right). a_{cube} is defined by the geometrical ionic radius of O^{2-} (1.38 Å). Changing the rare-earth elements changes the R-O bond lengths, and therefore provides a rough measure for the maximum solubility of Ce^{4+}.

Using this radius as r_{avg} in Eq. (1) provides an upper limit for the solubility limit of Ce^{4+} ions in $Nd_{2-x}Ce_xPdO_4$ to be $x \approx 0.7$. We should note here that the calculated solubility limits are much larger than the experimental solubility limits. Two reasons can be cited for this. First, the assumption that each ion can be represented as a rigid sphere with its corresponding ionic radius does not account for the actual ionic bond environment in a solid. Second, we ignored thermodynamic constraints of the ionic bond dynamics, while there are strong reasons to take the actual temperature dependency of the tolerance factor into account [74,75]. This sizable discrepancy can be seen in the case of the high-temperature superconductor $Nd_{2-x}Ce_xCuO_4$, where the calculated solubility limit is $x_{\max} \approx 0.7$ and is therefore about three times larger than the solubility limit determined experimentally [72]. Overall, one should keep in mind that the determination of the miscibility gap in incongruently melting materials is far from trivial and we will define the solubility limit by the appearance of CeO_2 precipitates.

Since the path towards a reliable theoretical model to determine the solubility limit [76] in a complex transition-metal oxide system such as $Nd_{2-x}Ce_xPdO_4$ is a tough task [77], our experimental results described below are sufficiently significant to draw an independent conclusion.

IV. RESULTS AND DISCUSSION

Drawing physically relevant conclusions from data measured on any material demands the highest crystal quality attainable. In Fig. 5, we plot a large section of the reciprocal space where diffraction spots of the MBE-grown single-crystalline Nd_2PdO_4 film are shown. Clearly, there are only diffraction spots visible associated to either Nd_2PdO_4 or the substrate. Moreover, the film is grown in a completely relaxed way on the $SrTiO_3$ substrate. The film thickness is ~160 nm, and the a-/c-axis lattice constants for Nd_2PdO_4 are $a_0 = 4.008$ Å

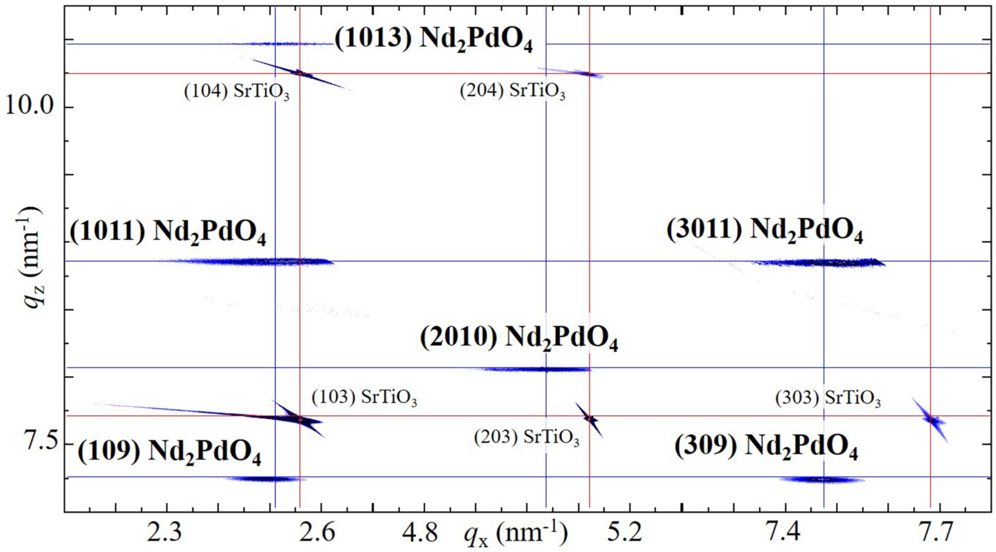

FIG. 5. The high-resolution reciprocal-space map (HRRSM) of the single-crystalline Nd_2PdO_4 film (film B). Nd_2PdO_4 is grown in a relaxed way on $SrTiO_3$ substrate with a lattice mismatch of 2.7 %. The $I4/mmm$ group theory considerations provide selection rules: $h + l + k = 2n$ (even number).

and $c_0 = 12.409$ Å. For La_2PdO_4 and Sm_2PdO_4, the lattice constants are also shown in Table III.

Similar to our earlier report [39], the resistivity behavior of Nd_2PdO_4 is insulating (Fig. 6) below 300 K. This is also true for La_2PdO_4 and Sm_2PdO_4, and the observed higher resistivity values (one order of magnitude) for La_2PdO_4 are a consequence of the higher affinity of La_2PdO_4 for stabilizing La_4PdO_7 [78]. Hereafter, we will therefore consider only Nd_2PdO_4 and $Nd_{2-x}Ce_xPdO_4$ to determine the electronic ground states and the Ce solubility limit.

Doping Ce into Nd_2PdO_4, resulting in $Nd_{2-x}Ce_xPdO_4$, not only enhances the electron count, but also distorts the host lattice. This distortion is a consequence of the significantly smaller ionic radius of Ce^{4+} (0.97 Å) than Nd^{3+} (1.109 Å), and therefore the determining factor of the solubility limit. We expect that the a- and c-axis lattice constants will shrink due to Vegard's law. While this is true for the c-axis lattice constants [Fig. 7(a)], the in-plane lattice constants remain unchanged over the doping range tested here ($0 \leqslant x < 0.3$) [Fig. 7(b)].

The electrons occupying the antibonding orbital ($4d_{x^2-y^2}$) cause an expansion of the Pd-O bond length. This expansion is compensated due to the smaller ionic radius of the Ce^{4+} ions. The doping-independent in-plane lattice constants strongly suggest that electron doping via Ce^{4+} substitution actually takes place. This trend coincides well with the lattice parameters reported for $Nd_{2-x}Ce_xPdO_4$ powder samples [68,69,79]. In contrast, the c-axis lattice constants reported for powder $Nd_{2-x}Ce_xPdO_4$ samples are always larger for a given Ce concentration than our films. Nonetheless, one should take into account that the full-width at half maximum (FWHM) values of the x-ray diffraction peaks of polycrystalline samples are broad and cause larger error bars. The FWHM values are a well-known measure for the coherent volume of the crystals and this is reflected in the overall conductivity values.

TABLE III. The a- and c-axis lattice constants for R_2PdO_4 ($R =$ La, Nd, and Sm) estimated from reciprocal-space maps. All films are grown completely relaxed, and both a-/c-axis lattice constants vary subject to Vegard's law. We should note that the error analysis of the lattice constants yields ±1%.

Composition	a_0(Å)	c_0(Å)
La_2PdO_4	4.083	12.705
Nd_2PdO_4	4.008	12.409
Sm_2PdO_4	3.980	12.297

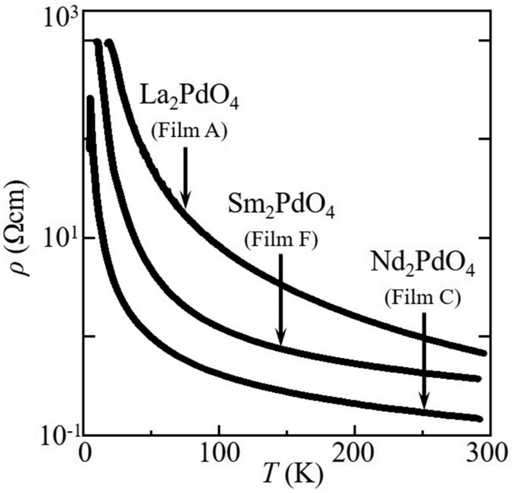

FIG. 6. The temperature dependencies of resistivity (ρ-T) for undoped R_2PdO_4 films ($R =$ La, Nd, and Sm). In single-crystalline R_2PdO_4 films, the resistivity values at 300 K range from 0.1 to 1 Ωcm. The resistivity values increase monotonically as the temperature decreases from 300 to 4.2 K. Note that the differences of the resistivities between undoped R_2PdO_4 films are due to the superior crystalline quality of Nd_2PdO_4 thin films and are not a consequence of the different R^{3+}.

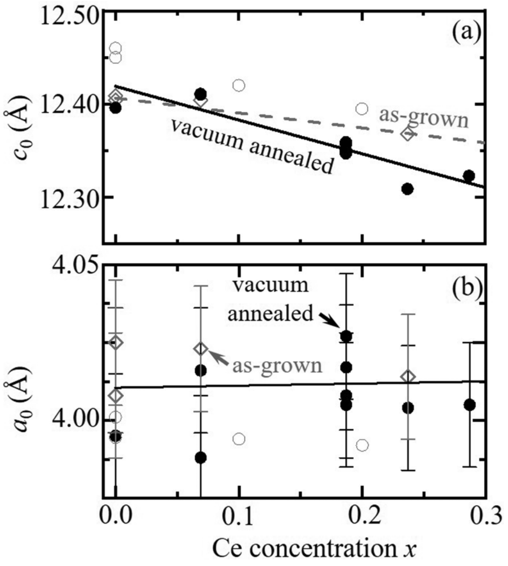

FIG. 7. Doping dependence of lattice parameters (a) c_0 and (b) a_0 of $Nd_{2-x}Ce_xPdO_4$ thin films grown on (001) $SrTiO_3$. As x increases, c_0 decreases for as-grown (open diamond) and vacuum annealed (filled circle) $Nd_{2-x}Ce_xPdO_4$ films. The Ce concentration dependence of a_0 is superimposed by the doping effect on the Pd-O bond length, and thus a_0 remains constant over the doping range investigated here. Data points of powder samples (open circles) have been taken from [67–69].

Within error bars, there are no significant differences of the c-axis lattice constants between our films and powder samples.

In the following, we will show how the additional doped charge carriers influence the electronic conduction in $Nd_{2-x}Ce_xPdO_4$ single-crystalline thin films. From insulating Nd_2PdO_4 with an expected band gap of ~0.8–2.0 eV, we assume that the electron doping shifts the Fermi level closer to the $4d_{x^2-y^2}$ level. The elevated Fermi level results in a smaller activation energy, and therefore we expect that this results in an enhanced electronic conductivity (Fig. 3). In Fig. 8, we plot the temperature dependency of the resistivity (ρ-T) for $x = 0.00$, 0.07, and 0.24 of vacuum annealed $Nd_{2-x}Ce_xPdO_4$. In the undoped case, the temperature dependence is, as expected, insulating with the resistivity value of ~100 mΩcm at 300 K. For $x = 0.07$, the resistivity value drops to ~30 mΩcm at 300 K, while the system still remains insulating. Further doping does not lower the resistivity value significantly.

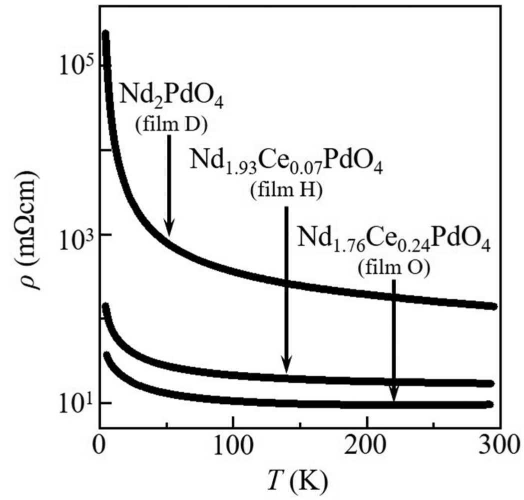

FIG. 8. The temperature dependencies of the resistivity (ρ-T) for vacuum annealed $Nd_{2-x}Ce_xPdO_4$ films ($x = 0.00$, 0.07, and 0.24). As the Ce concentration increases, the electronic conductivities increase. For $x \approx 0.24$ (film O), $Nd_{2-x}Ce_xPdO_4$ shows metallic conduction down to the inflection temperature $T_u \approx 240$ K and this is detailed in Fig. 10.

The insulating behavior seen in $Nd_{2-x}Ce_xPdO_4$ films raises the question of the mechanism of the charge carrier transport. In the absence of an antiferromagnetic ground state [69], as seen in cuprates, the charge carrier transport in two-dimensional systems is preferably motivated by variable-range hopping (VRH) [80]. The temperature dependence of the resistivity in a VRH scenario is given by

$$\rho \propto \exp\left[\left(\frac{T_0}{T}\right)^{\frac{1}{(d+1)}}\right], \tag{2}$$

where T_0 and d are the characteristic temperature and the dimension of the system, respectively. The characteristic temperature T_0 is a measure of the localization length ξ through

$$T_0 \propto 1/k_B D \xi^d, \tag{3}$$

where D is the density of states at the Fermi energy. Certainly the system discussed here is a layered system with two-dimensional PdO_2 planes, and therefore the electronic transport is expected to be two dimensional as well. We tested this hypothesis by plotting $\log_{10}(\rho)$ as a function of $T^{-\frac{1}{3}}$ in Fig. 9. Regardless of the values of x, the resistivity deviations $\Delta\rho$ are less than 1% over the entire temperature range. Here, $\Delta\rho$ is defined as

$$\Delta\rho = A \times \exp\left[\left(\frac{T_0}{T}\right)^{\frac{1}{3}}\right] - \rho, \tag{4}$$

where ρ is the experimentally determined resistivity value and A is a constant. The small deviation of $\Delta\rho$ over the entire temperature range supports that the charge carrier activation in $Nd_{2-x}Ce_xPdO_4$ takes place in two dimensions (2D) via a hopping mechanism.

For $0.19 \leqslant x \leqslant 0.24$ in $Nd_{2-x}Ce_xPdO_4$, the insulating behavior disappears. Instead, $Nd_{2-x}Ce_xPdO_4$ is metallic down to T_u of 210 K (Fig. 10, film K), where T_u is the temperature of inflection between the metallic and insulating range. We confirmed the metallic conduction ($d\rho/dT > 0$) between 400 K and T_u with $d\rho/dT \approx 3$ $\mu\Omega$cm/K. However, further doping does not enhance the metallic conduction owing to the nearby Ce solubility limit in $Nd_{2-x}Ce_xPdO_4$. For example, in Fig. 10, for film Q which contains Ce concentration $x = 0.29$, the resistivity is about three times higher than film K with Ce concentration $x = 0.19$. The excessive Ce forms CeO_2, $(Nd,Ce)_2O_3$, and $(Ce,Pd)O_2$ acting as a insulating matrix embedding $Nd_{2-x}Ce_xPdO_4$ and the existence of these impurity phases in film Q (Fig. 10) was confirmed by x-ray diffraction. Consequently, the resistivity values increase, as shown in

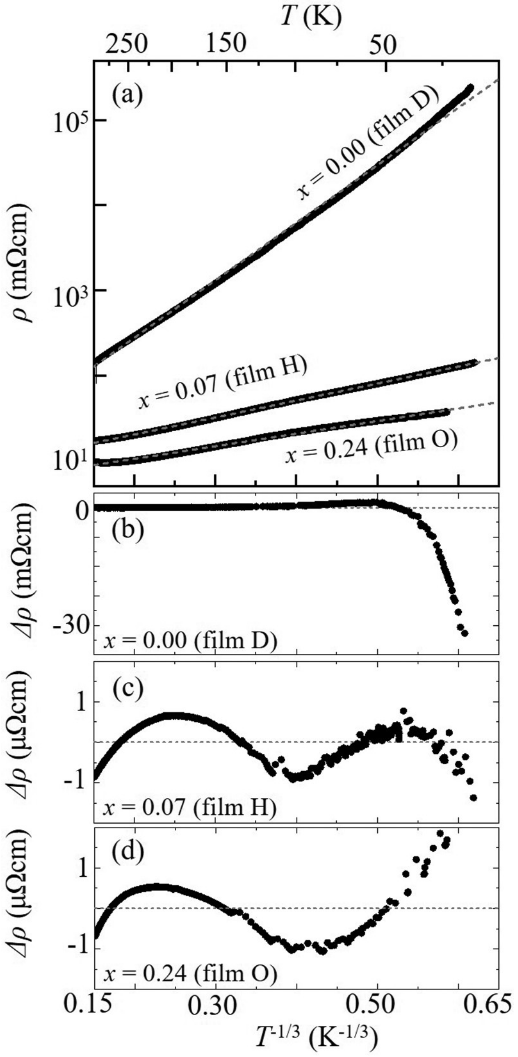

FIG. 9. (a) A plot of $\log_{10}(\rho)$ as a function of $T^{-\frac{1}{3}}$ for vacuum annealed $Nd_{2-x}Ce_xPdO_4$ films with $x = 0.00$, 0.07, and 0.24. (b)–(d) The resistivity deviation $\Delta\rho$ [see Eq. (4)] from VRH behavior for $x = 0.00$, 0.07, and 0.24, respectively. Note that $\Delta\rho$ is less than 1%, regardless of x.

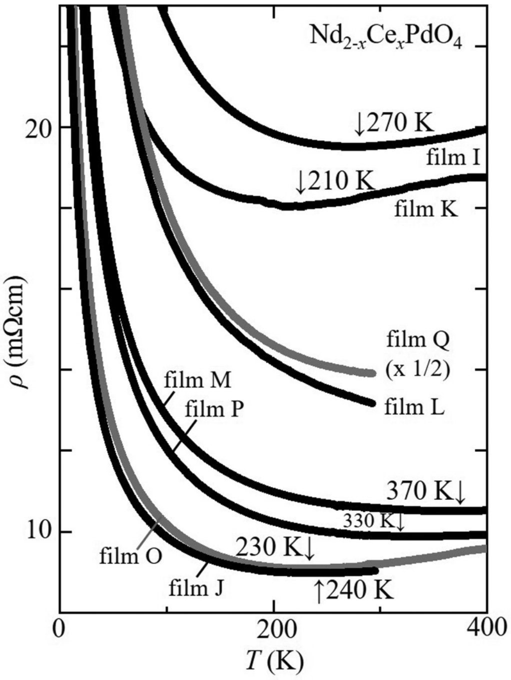

FIG. 10. The ρ-T plots for $Nd_{2-x}Ce_xPdO_4$ films ($x \geqslant 0.19$) at the crossover from metallic to insulating conduction (films I, J, K, M, O, and P). For comparison, the ρ-T curves for films L and Q are also shown. All films shown here have been vacuum annealed. The crossover temperature (T_u) (marked by arrows) ranges from 210 to 370 K. For films L and Q, the absolute resistivity values are similar to film I, J, K, M, O, and P, though metallic behavior does not appear. The $Nd_{2-x}Ce_xPdO_4$ films with T_u show typical resistivity of 10 to 20 mΩcm at 300 K.

Fig. 10. This resistivity enhancement, however, is not due to doping but impurity phase formation. In the following, we will not consider $Nd_{2-x}Ce_xPdO_4$ films with $x > 0.24$. The films we have been discussing are made by the same procedure, namely, after their synthesis the films have been subject under ultrahigh vacuum (see Table II). It is well known that the complex transition-metal oxides are sensitive to their synthesis and annealing history. As expected, this also holds for the absolute resistivity values of $Nd_{2-x}Ce_xPdO_4$ thin films (see Fig. 8). The 2D VRH scenario fits also for as-grown $Nd_{2-x}Ce_xPdO_4$ films, while their resistivity values are significantly higher (several hundred mΩcm at 300 K).

The reduction of resistivity values in $Nd_{2-x}Ce_xPdO_4$ by annealing can be explained by the following. First of all, the limiting factors in any diffusion process are temperature, time, and fugacity. Given the annealing condition under ultrahigh vacuum remains constant, the fugacity will not change. That leaves us with two parameters. Considering the temperature range, it is limited by the dissociation temperatures of Nd_2PdO_4 or $Nd_{2-x}Ce_xPdO_4$ on the upper end, and the formation temperature on the lower end. The annealing temperature used here (see Table II) have been chosen to exactly fulfill those requirements. During the growth, the deposited Ce oxidizes into CeO_2 and accumulates along grain boundaries of $Nd_{2-x}Ce_xPdO_4$, partially. As a result, the dependency of the c-axis lattice constant c_0 on the Ce concentration in the as-grown $Nd_{2-x}Ce_xPdO_4$ (Fig. 7) is languid. During the annealing treatment, CeO_2 partially diffuses from the grain boundaries into the $Nd_{2-x}Ce_xPdO_4$ lattice and this is reflected by the prominent c_0 dependence on the Ce concentration (Fig. 7). As a consequence, the electronic conductivity is enhanced. At the same time, however, the annealing process seems to create palladium vacancies and these vacancies compensate the doped electron charge carriers.

This scenario is further supported by our XPS analysis for $Nd_{2-x}Ce_xPdO_4$ for $x = 0.00$ and 0.19. In PdO, the energy positions of the Pd $3d_{\frac{5}{2}}$ and $3d_{\frac{3}{2}}$ peaks are 337.2 and 342.5 eV, respectively [81], whereas for elemental palladium the Pd $3d_{\frac{5}{2}}$ level is at 335.4 eV. In PdO, the square-planar coordinated Pd^{2+} ions form perpendicularly overlapping one-dimensional chains, in contrast to Nd_2PdO_4. Nonetheless, the coordination symmetry is identical in both compounds and we therefore do not expect a significant variation of the Pd binding energy. Upon doping (see Fig. 11), the binding energy [81,82] of the

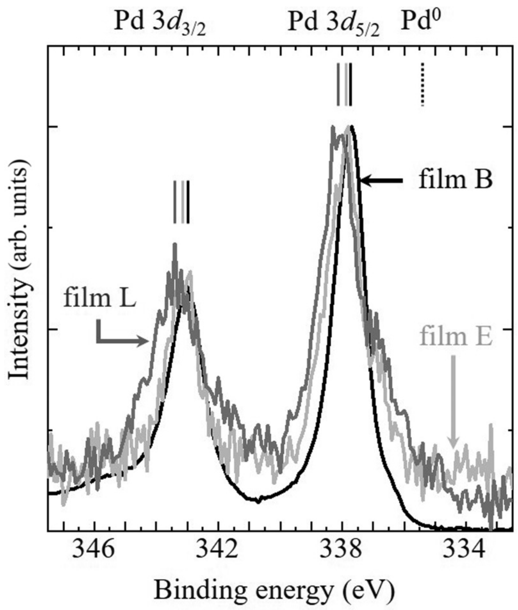

FIG. 11. Plot of the normalized x-ray photoemission spectra showing the evolution of the Pd^{2+} binding energies in $Nd_{2-x}Ce_xPdO_4$ for films B, E, and L. The shift of the binding energies by Ce substitution (film L) and vacuum annealing (film E) compared to as-grown undoped Nd_2PdO_4 film (film B). Upon Ce doping, the binding energy of Pd 3*d* states shifts toward higher energies. The vacuum annealing process gives a similar effect on $Nd_{2-x}Ce_xPdO_4$. On the other hand, the appearance of the Pd metal component implies partial decomposition of the $Nd_{2-x}Ce_xPdO_4$ phase by vacuum annealing.

Pd 3*d* level shifts toward higher binding energies. Interestingly, however, vacuum annealing has a similar influence on $Nd_{2-x}Ce_xPdO_4$ compared to $x = 0.19$ as-grown and vacuum annealed samples. For the solid state, the binding energy can be written as

$$E_b(j) = -\epsilon_{\mathrm{HF}}^{\mathrm{atom}} + V_a(j) - R_a(j) + V_{ea}(j) - R_{ea}(j) - \Phi, \qquad (5)$$

where $-\epsilon_{\mathrm{HF}}^{\mathrm{atom}}$, $V_a(j)$, $R_a(j)$, $V_{ea}(j)$, $R_{ea}(j)$, and Φ are the Hartree-Fock energy of the free atom, shift of $-\epsilon_{\mathrm{HF}}$ due to valence charges, intra-atomic relaxation energy, Madelung potential, extra-atomic relaxation energy, and work function, respectively. The shift of the binding energy, $\Delta E_b \cong \Delta(V_a + V_{ea}) - \Delta R_{ea}$, depends on the change of the valence charge ($\propto \frac{\Delta q}{r}$), the Madelung constant, and the response of the generated core hole. Without limitations of generality, a shift towards higher binding energies is commonly associated with a higher oxidizing state. For $Nd_{2-x}Ce_xPdO_4$, the shift towards higher binding energies coincides with a significant (about 75%) loss of spectral weight of the Pd $3d_{\frac{5}{2}}$ and $3d_{\frac{3}{2}}$ peaks at 337 and 343 eV, when compared to the undoped and as-grown Nd_2PdO_4 thin film. At the same time, spectral weight at the 335.4 eV increases, indicating the formation of elemental Pd. Using published XPS data [83] on the positions of the $3d_{\frac{5}{2}}$ and $3d_{\frac{3}{2}}$ positions (Π), and letting Υ be the valence state of the palladium, we find the following relations:

TABLE IV. Stoichiometries determined by inductively coupled plasma analysis for as-grown and vacuum annealed $Nd_{2-x}Ce_xPdO_4$ thin films.

Sample	(Nd+Ce) : Pd
$x = 0.00$, as-grown	2 : 0.985
$x = 0.00$, vacuum annealed	2 : 0.977
$x = 0.07$, vacuum annealed	2 : 0.956
$x = 0.19$, vacuum annealed	2 : 0.939
$x = 0.24$, vacuum annealed	2 : 0.962

$$\Pi_{\frac{5}{2}} \approx (335.156 \pm 0.322)\,\mathrm{eV} + 1.00536 \times \Upsilon\big(3d_{\frac{5}{2}}\big), \qquad (6)$$

$$\Pi_{\frac{3}{2}} \approx (340.373 \pm 0.391)\,\mathrm{eV} + 1.20125 \times \Upsilon\big(3d_{\frac{3}{2}}\big). \qquad (7)$$

Our analysis of the XPS spectra of Nd_2PdO_4 and $Nd_{2-x}Ce_xPdO_4$ films (Fig. 11) [84] results in a noticeable shift of the binding energies from 337.77 eV (film B) → 337.92 eV (film E) → 338.07 eV (film L). Using Eqs. (6) and (7), the formal oxidation state of palladium in the as-grown and undoped condition is larger than +2. It is noteworthy that the influence of the annealing process on the oxidation state is comparable to that observed by doping. Unfortunately, the vacuum annealing process is not flawless and it results in partial decomposition of $Nd_{2-x}Ce_xPdO_4$ and the appearance of the Pd $3d^0$ spectral weight contribution suggests that the vacuum annealing process, at least to some extent, is in favor of the following decomposition reaction: $Nd_{2-x}Ce_xPdO_4 \rightarrow Pd + (Nd,Ce)_2O_3$. In addition, if PdO is formed during the annealing process, it would evaporate from the film due to its high vapor pressure [85–88]. This in turn results in a palladium deficit $Nd_{2-x}Ce_xPd_{1-y}O_4$ film. As the presence of Pd vacancies in the PdO_2 planes has a strong influence on the electronic conduction in $Nd_{2-x}Ce_xPdO_4$, we tested their existences by ICP analysis and the results are listed in Table IV. In the as-grown state, the Pd stoichiometry is very close to the expected value of 1.000. Upon vacuum annealing, however, a loss of more than 1% Pd is detected. This loss of Pd is also traced for Ce-doped samples and we find that the Pd loss extends over the entire doping range investigated here. Further, we state that the loss of Pd increases for higher doping concentrations up to the point when the solubility limit is reached. We expect that such a loss of Pd influences the XPS spectra and the influence may not be subtle.

Consequently, the combined electronic contributions of Ce doping (electron doping), Pd vacancies (hole doping), and vacuum annealing (more hole doping due to higher Pd vacancy concentrations [89]) of $Nd_{2-x}Ce_xPdO_4$ result in an electronic state that allows for metallic conduction above T_u. The loss of Pd results in the manipulation of electronic states in unexpected ways and thus impedes the electronic transport in the low-temperature limit. The process underlying the annealing procedure is sensitive to minute variation of the as-grown films. For example, the synthesis and annealing conditions of films K and L are identical, though only film K shows a metallic conduction with $T_u \approx 210$ K (Fig. 10). Moreover, the film thickness does not play a role in the induction of the metallic conduction, e.g., thicknesses of films

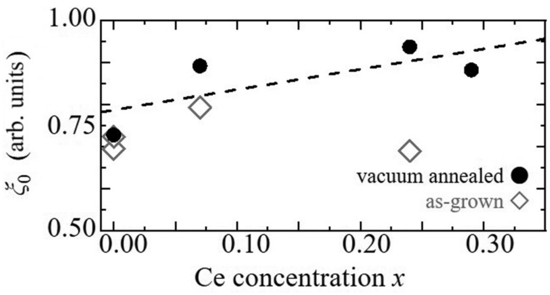

FIG. 12. Normalized localization length ξ_0 as a function of Ce concentration x. By Ce doping, ξ_0 becomes longer, i.e., the system becomes less localized for vacuum annealed $Nd_{2-x}Ce_xPdO_4$ films, whereas the values of ξ_0 for as-grown films remain almost constant. The dashed line is a linear fit to all of the data points of the vacuum annealed samples.

I and J are 80 and 160 nm, respectively. Nonetheless, both films show metallic conduction above T_u with $x = 0.19$.

Using Eq. (3) with proportionality constant 1, the localization length ξ becomes a normalized localization length ξ_0. The trend shown in Fig. 12 indicates that the ξ_0 increases as x increases. At $x = 0.24$, the value of ξ_0 is 30% larger than at $x = 0$. While this enhancement is partially due to our assumption of a constant density of states at the Fermi level, it also reflects the underlying mechanism of delocalization. One would expect that an increasing localization length results in a shift of T_u toward lower temperatures. For $Nd_{2-x}Ce_xPdO_4$ films which show metallic conduction, we plot the values of T_u as a function of ξ_0 in Fig. 13. Indeed, T_u decreases as ξ_0 increases. The $Nd_{2-x}Ce_xPdO_4$ films shown in Fig. 13 have all been vacuum annealed and with the Ce concentration $0.19 \leqslant x \leqslant 0.24$. To extrapolate the necessary Ce concentration that is mandatory to make the entire system into a metal, we assume two conditions. One is that the hopping length for a metallic state in $Nd_{2-x}Ce_xPdO_4$ is longer than the Pd-Pd distance of ~4 Å, and that T_u varies linearly with ξ_0 over a small range. This would give a Ce concentration of $x \approx 0.45$ to induce bulk metallic conduction. During our attempts to reach the experimental solubility limit of Ce in $Nd_{2-x}Ce_xPdO_4$, we noticed, however, that the $x = 0.45$ is far beyond this point.

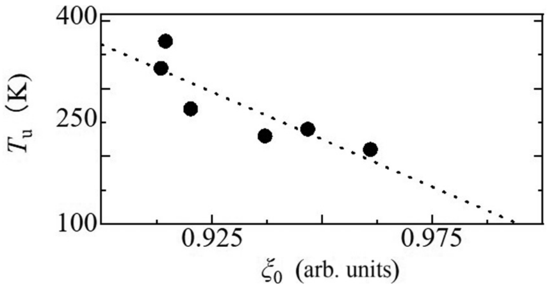

FIG. 13. The relationship between T_u and ξ_0. As ξ_0 becomes longer, the values of T_u decreases. The required Ce concentration for fully metallic $Nd_{2-x}Ce_xPdO_4$ ($T_u = 0$) is estimated to be $x \approx 0.45$; meanwhile, the value of T_u is estimated to be ~850 K for Nd_2PdO_4. The dotted line is a linear fit to all of the data points.

In this context, we estimated T_u for undoped Nd_2PdO_4 to be $T_u \approx 850$ K. This temperature corresponds to an activation energy of ~ 73 meV, and this is comparable to the findings reported by Shibasaki *et al.* [69].

Finally, we will discuss the attendant circumstances of the observed metallic conduction in $Nd_{2-x}Ce_xPdO_4$. While the resistivity values for the powder samples are typically ~3–4 orders of magnitude higher than the resistivity values reported here, the higher crystal quality of our $Nd_{2-x}Ce_xPdO_4$ thin-film samples led to the same insulating electronic ground state in Nd_2PdO_4. Nonetheless, Shibasaki *et al.* managed to derive a carrier concentration from Seebeck measurements of $Nd_{2-x}Ce_xPdO_4$ samples of $n = 1.6 \times 10^{21}$ cm^{-3} [69]. As shown by our XPS results, the doped charge carriers shift the Pd 3*d* level toward higher binding energies. Apparently, this shift is not subject to Ce doping or the vacuum annealing treatment as both processes would result in a reduction of the formal valence state of palladium and the binding energy should, therefore, be reduced. While one might be able to construct a scenario in which electron doping in layered palladates accounts for the effects seen here, material-related parameters are far more influential, i.e., the apparent off-stoichiometry induced by the annealing process. On one hand, electron charge carriers are doped via Ce, whereas the formation of Pd vacancies amount to a problem as they compensate and even overcompensate those charge carriers. In fact, we see a shift of the Pd binding energy of ~0.3 eV upon Ce doping and vacuum annealing (Fig. 11) and we can write the formal valence state of Pd as $2 - x + \eta$, where η is the defect concentration of Pd. If η is larger than x, the formal valency of Pd increases and so does the binding energy of the Pd 3*d*—and this is what is observed in $Nd_{2-x}Ce_xPdO_4$. The apparent enhancement of electronic conduction is therefore driven by hole carriers which are induced via Pd vacancies [90]. This result is in contrast to the negative Seebeck coefficient reported by Shibasaki *et al.* [69]. A situation where high doping level concentrations cause defects on other crystallographic sites has been reported for other widely studied band insulators, e.g., GaAs [91]. For metals, it is key that the mean-free-path length ℓ is, at the very least, longer than the lattice constant (~ 4 Å for $Nd_{2-x}Ce_xPdO_4$). In the simplest case, the electronic conductivity of a PdO_2 plane in $Nd_{2-x}Ce_xPdO_4$ is $\sigma_{\mathrm{PdO}_2} = \rho_{\mathrm{PdO}_2}^{-1} = ne^2\tau_e m^{-1}$, where m is the effective electron mass and $\tau_e = m\ell(\hbar k_F)^{-1}$ is the electron scattering rate. Assuming a two-dimensional parabolic energy dispersion $2\pi n = k_F^2$, the electronic conductivity can be written as $\sigma_{\mathrm{PdO}_2} = e^2h^{-1}(k_F\ell)$. The Fermi wave vector would become $k_F \approx \frac{\pi}{a} \approx 0.78$ Å^{-1}. Even for film J, which shows the lowest resistivity value among the $Nd_{2-x}Ce_xPdO_4$ films discussed here, $\ell \approx 2.6$ Å at T_u and this is below the Ioffe-Regel limit [92]. It remains to be seen if the higher defect concentrations introduced by Ce doping or the higher charge carrier concentration are primarily responsible for the weak influence on the electronic conduction. We may speculate that the vacuum annealing procedures presented here may be subject to further optimization in order to prevent the partial decomposition of $Nd_{2-x}Ce_xPdO_4$ into Pd and rare-earth oxides as seen in the XPS result (see Fig. 11). Ultimately, our synthesis method of MBE empowered us to shift the Ce solubility limit as far as $x \approx 0.3$. Upon higher doping concentrations, the Pd vacancy concentrations also increase notably and the metallic conduction seen in the palladates here, having infinite two-dimensional PdO_2 planes, is driven via hole carriers in a high-defect environment [93]. Our finding that T_u becomes lower as the normalized localization length ξ_0 becomes longer for the band insulator $Nd_{2-x}Ce_xPdO_4$ emphasizes the distinction from other 4*d* transition-metal oxides where the transition-metal ions are octahedral coordinated. For square-planar coordinated Pd^{2+} ions, the bonding orbitals are dsp^2 and this agrees well with other palladates (see Fig. 1), where hole doping is key to trigger a transition from an insulating ground state towards a metal. Our method might encourage further research on the synthesis of $Nd_{2-x}Ce_xPdO_4$ in order to optimize the annealing process further. One might also keep an eye on the possibility that hole doping rather than electron doping into Pd-defect-free Nd_2PdO_4 may result in a metallic state, e.g., field-effect doping [94]. On a final note, one might be intrigued as to what extent oxygen vacancies, which are linked to palladium defects, might play a role in the electronic conduction in the R_2PdO_4 system. Certainly, oxygen vacancies in PdO_2 layers hamper the two-dimensional electronic conduction while additional electron charge carriers are doped. We therefore encourage further investigations on Pd-defect-free samples to clarify the influence of oxygen vacancies too.

ACKNOWLEDGMENTS

We thank Takayuki Ikeda for patiently measuring the band gap of $Nd_{2-x}Ce_xPdO_4$ via EELS. We also thank Kazuhide Kumakura for stimulating discussions.

---

[1] W. Siemons, G. Koster, A. Vailionis, H. Yamamoto, D. H. A. Blank, and M. R. Beasley, Dependence of the electronic structure of $SrRuO_3$ and its degree of correlation on cation off-stoichiometry, Phys. Rev. B **76**, 075126 (2007).

[2] Y. Krockenberger, M. Uchida, K. S. Takahashi, M. Nakamura, M. Kawasaki, and Y. Tokura, Growth of superconducting Sr_2RuO_4 thin films, Appl. Phys. Lett. **97**, 082502 (2010).

[3] M. Uchida, M. Ide, H. Watanabe, K. S. Takahashi, Y. Tokura, and M. Kawasaki, Molecular beam epitaxy growth of superconducting Sr_2RuO_4 films, APL Mater. **5**, 106108 (2017).

[4] A. Radetinac, K. S. Takahashi, L. Alff, M. Kawasaki, and Y. Tokura, Single-crystalline $CaMoO_3$ and $SrMoO_3$ films grown by pulsed laser deposition in a reductive atmosphere, Appl. Phys. Express **3**, 073003 (2010).

[5] J. S. Lee, Y. Krockenberger, K. S. Takahashi, M. Kawasaki, and Y. Tokura, Insulator-metal transition driven by change of doping and spin-orbit interaction in Sr_2IrO_4, Phys. Rev. B **85**, 035101 (2012).

[6] Seung-Joo Kim, S. Lemaux, G. Demazeau, Jong-Young Kim, and Jin-Ho Choy, X-ray absorption spectroscopic study on $LaPdO_3$, J. Mater. Chem. **12**, 995 (2002).

[7] A. P. Mackenzie, The properties of ultrapure delafossite metals, Rep. Prog. Phys. **80**, 032501 (2017).

[8] J. P. Attfield and G. Férey, Structural correlations within the lanthanum palladium oxide family, J. Solid State Chem. **80**, 286 (1989).

[9] R. Uriu, D. Shimada, and N. Tsuda, Metal to insulator transition in $Pd_{1-x}Li_xO$, J. Phys. Soc. Jpn. **60**, 2479 (1991).

[10] M. Andersson, J. Grins, and M. Nygren, Structure, thermodynamic, and magnetic properties of Ln_4PdO_7 with Ln= La, Nd, Sm, Eu, and Gd, J. Solid State Chem. **146**, 428 (1999).

[11] R. A. Matula, Electrical resistivity of copper, gold, palladium, and silver, J. Phys. Chem. Ref. Data **8**, 1147 (1979).

[12] S. Dutta, K. Sankaran, K. Moors, G. Pourtois, S. V. Elshocht, J. Bömmels, W. Vandervorst, Z. Tőkei, and C. Adelmann, Thickness dependence of the resistivity of platinum-group metal thin films, J. Appl. Phys. **122**, 025107 (2017).

[13] E. A. Owen and E. L. Yates, XLI. Precision measurements of crystal parameters, London Edinburgh Dublin Philos. Mag. J. Sci. **15**, 472 (1933).

[14] W. P. Davey, Precision measurements of the lattice constants of twelve common metals, Phys. Rev. **25**, 753 (1925).

[15] G. Bredig and R. Allolio, Z. Phys. Chem. **126**, 41 (2018).

[16] R. D. Shannon, C. T. Prewitt, and D. B. Rogers, Chemistry of noble metal oxides. II. Crystal structures of platinum cobalt dioxide, palladium cobalt dioxide, coppper iron dioxide, and silver iron dioxide, Inorg. Chem. **10**, 719 (1971).

[17] M. Tanaka, M. Hasegawa, and H. Takei, Growth and anisotropic physical properties of $PdCoO_2$ single crystals, J. Phys. Soc. Jpn. **65**, 3973 (1996).

[18] Han-Jin Noh, J. Jeong, B. Chang, D. Jeong, H. S. Moon, E.-J. Cho, J. M. Ok, J. Sung Kim, K. Kim, B. I. Min, Han-Koo Lee, Jae-Young Kim, Byeong-Gyu Park, Hyeong-Do Kim, and Seongsu Lee, Direct observation of localized spin antiferromagnetic transition in $PdCrO_2$ by angle-resolved photoemission spectroscopy, Sci. Rep. **4**, 3680 (2014).

[19] H. Takatsu and Y. Maeno, Single crystal growth of the metallic triangular-lattice antiferromagnet $PdCrO_2$, J. Cryst. Growth **312**, 3461 (2010).

[20] R. D. Shannon, D. B. Rogers, and C. T. Prewitt, Chemistry of noble metal oxides. I. Syntheses and properties of ABO_2 delafossite compounds, Inorg. Chem. **10**, 713 (1971).

[21] P. Kushwaha, H. Borrmann, S. Khim, H. Rosner, P. J. W. Moll, D. A. Sokolov, V. Sunko, Yu. Grin, and A. P. Mackenzie, Single crystal growth, structure, and electronic properties of metallic delafossite $PdRhO_2$, Cryst. Growth Des. **17**, 4144 (2017).

[22] T. C. Ozawa, A. Matsushita, Y. Hidaka, T. Taniguchi, S. Mizusaki, Y. Nagata, Y. Noro, and H. Samata, Synthesis and characterization of electron and hole doped ternary palladium oxide: $Sr_{1-x}A_xPd_3O_4$ (A=Na, Bi), J. Alloys Compd. **448**, 77 (2008).

[23] Hans-Conrad zur Loye, P. L. Smallwood, and M. D. Smith, Flux synthesis of alkaline earth palladates, J. Cryst. Growth **216**, 299 (2000).

[24] T. Taniguchi, Y. Nagata, T. C. Ozawa, M. Sato, Y. Noro, T. Uchida, and H. Samata, Insulator-metal transition induced in $Sr_{1-x}Na_xPd_3O_4$ for small Na-substitutions, J. Alloys Compd. **373**, 67 (2004).

[25] K. Itoh and N. Tsuda, Metal to semiconductor like transition for sintered $Ca_{1-x}Na_xPd_3O_4$, Solid State Commun. **109**, 715 (1999).

[26] S. Ichikawa and I. Terasaki, Metal-insulator transition in $Ca_{1-x}Li_xPd_3O_4$, Phys. Rev. B **68**, 233101 (2003).

[27] R. V. Panin, N. R. Khasanova, A. M. Abakumov, E. V. Antipov, G. V. Tendeloo, and W. Schnelle, Synthesis and crystal structure of the palladium oxides $NaPd_3O_4$, Na_2PdO_3 and $K_3Pd_2O_4$, J. Solid State Chem. **180**, 1566 (2007).

[28] Ken-ichi Machida, M. Enyo, Gin-ya Adachi, and J. Shiokawa, Synthesis and electrocatalytic properties of rare earth platinum or palladium bronzes, Bull. Chem. Soc. Jpn. **60**, 411 (1987).

[29] H. K. Müller-Buschbaum and R. Arpe, About Bi_2PdO_4, Z. Naturforsch. B **31**, 1708 (2004).

[30] N. Bettahar, P. Conflant, and F. Abraham, Effect of copper substitution on the electrical transport properties of $(Bi, Pb)_2MO_4$ ($M = Pd, Pt$) linear chain compounds, J. Alloys Compd. **188**, 211 (1992).

[31] Bai-Hao Chen, D. Walker, and B. A. Scott, Crystal chemistry of $LuPd_2O_4$ and other spinel-related $NdCu_2O_4-LaPd_2O_4$-type compounds, Chem. Mater. **9**, 1700 (1997).

[32] G. Krämer, E. Hägele, N. Wagner, and M. Jansen, Untersuchungen zu struktur und physikalischen eigenschaften von oxiden der $LaPd_2O_4$-familie, Z. Anorg. Allg. Chem. **622**, 1027 (1996).

[33] M. Schreyer and M. Jansen, Synthesis, structure and properties of Ag_2PdO_2, Solid State Sci. **3**, 25 (2001).

[34] L. M. Misch, Platinum group metal oxides for heterogeneous catalysis: Novel synthesis and advanced characterization, CiteSeer, Ph.D. thesis, 2014.

[35] Y. Laligant, A. L. Bail, and G. Ferey, Complex palladium oxides. V. Crystal structure of $LiBiPd_2O_4$: An example of three different fourfold coordinations of cations, J. Solid State Chem. **81**, 58 (1989).

[36] H. D. Wasel-Nielen and R. Hoppe, Phases in the CaO/PdO and SrO/PdO systems, Z. Anorg. Allg. Chem. **375**, 209 (1970).

[37] Y. Nagata, T. Taniguchi, G. Tanaka, M Satho, and H Samata, Magnetic properties of $Sr_2Pd_{1-x}M_xO_3$ (M=Co, Cu), J. Alloys Compd. **346**, 50 (2002).

[38] L. K. Lamontagne, G. Laurita, M. W. Gaultois, M. Knight, L. Ghadbeigi, T. D. Sparks, M. E. Gruner, R. Pentcheva, C. M. Brown, and R. Seshadri, High thermopower with metallic conductivity in p-type Li-substituted $PbPdO_2$, Chem. Mater. **28**, 3367 (2016).

[39] Y. Nanao, A. Ikeda, M. Naito, H. Yamamoto, K. Kumakura, and Y. Krockenberger, Molecular beam epitaxy of Nd_2PdO_4 thin films, AIP Adv. **7**, 075006 (2017).

[40] J. A. Kurzman, Xiaoying Ouyang, W. B. Im, J. Li, J. Hu, S. L. Scott, and R. Seshadri, La_4LiAuO_8 and La_2BaPdO_5: Comparing two highly stable d^8 square-planar oxides, Inorg. Chem. **49**, 4670 (2010).

[41] T. Taniguchi, Y. Kawaji, T. C. Ozawa, Y. Nagata, Y. Noro, H. Samata, and M. D. Lan, Antiferromagnetism of R_2BaPdO_5 (R=La, Nd, Pr, Sm, Eu, Gd, Dy, Ho), J. Alloys Compd. **386**, 63 (2005).

[42] T. C. Ozawa, T. Taniguchi, Y. Kawaji, Y. Nagata, Y. Noro, H. Samata, and S. Takayanagi, Spin frustration and antiferromagnetic long range order in R_2BaPdO_5 (R= rare earth), Phys. Lett. A **337**, 130 (2005).

[43] R. V. Panin, N. R. Khasanova, C. Bougerol, W. Schnelle, G. V. Tendeloo, and E. V. Antipov, Ordering of Pd^{2+} and Pd^{4+} in the mixed-valent palladate K_2PdO_3, Inorg. Chem. **49**, 1295 (2010).

[44] M. Wilhelm and R. Hoppe, Zur Kenntnis von $Na_2Pd_3O_4$, Zeitschrift für anorganische und allgemeine Chemie **409**, 60 (1974).

[45] Th. Hansen and H. K. Müller-Buschbaum, On the first earth-alkaline mercury palladate (II,IV): $Ba_2Hg_3Pd_5^{2+}Pd_2^{4+}O_{14}$, Z. Anorg. Allg. Chem. **616**, 67 (1992).

[46] Y. Wang, D. Walker, B.-H. Chen, and B. A. Scott, High-pressure synthesis of one-dimensional alkaline-earth palladates, J. Alloys Compd. **285**, 98 (1999).

[47] G. Demazeau, I. Omeran, M. Pouchard, and P. Hagenmuller, On the synthesis of a new palladate (+IV) phase: Zn_2PdO_4, Mater. Res. Bull. **11**, 1449 (1976).

[48] M.-B. Hanskarl, On the crystal chemistry of palladates, Z. Anorg. Allg. Chem. **631**, 239 (2005).

[49] D. B. Rogers, R. D. Shannon, and J. L. Gillson, Crystal growth and semiconductivity of palladium oxide, J. Solid State Chem. **3**, 314 (1971).

[50] H. Eisaki, S. Uchida, T. Mizokawa, H. Namatame, A. Fujimori, J. van Elp, P. Kuiper, G. A. Sawatzky, S. Hosoya, and H. Katayama-Yoshida, Electronic structure of $La_{2-x}Sr_xNiO_4$ studied by photoemission and inverse-photoemission spectroscopy, Phys. Rev. B **45**, 12513 (1992).

[51] G. A. Sawatzky and J. W. Allen, Magnitude and Origin of the Band Gap in NiO, Phys. Rev. Lett. **53**, 2339 (1984).

[52] R. J. Cava, B. Batlogg, T. T. Palstra, J. J. Krajewski, W. F. Peck, Jr., A. P. Ramirez, and L. W. Rupp, Jr., Magnetic and electrical properties of $La_{2-x}Sr_xNiO_{4\pm\delta}$, Phys. Rev. B **43**, 1229 (1991).

[53] M. W. Haverkort, I. S. Elfimov, L. H. Tjeng, G. A. Sawatzky, and A. Damascelli, Strong Spin-Orbit Coupling Effects on the Fermi Surface of Sr_2RuO_4 and Sr_2RhO_4, Phys. Rev. Lett. **101**, 026406 (2008).

[54] A. Khan, Z. Ali, I. Khan, and I. Ahmad, First-principles study of electronic structure, mechanical, and thermoelectric properties of ternary palladates $CdPd_3O_4$ and $TlPd_3O_4$, J. Electron. Mater. **47**, 1871 (2018).

[55] G. L. Stamokostas and G. A. Fiete, Mixing of $t_{2g} - e_g$ orbitals in 4d and 5d transition metal oxides, Phys. Rev. B **97**, 085150 (2018).

[56] V. Val. Sobolev, D. O. Mordas, and V. V. Sobolev, Optical spectra of palladium oxide, Glass Phys. Chem. **29**, 360 (2003).

[57] R. A. van Santen, I. Tranca, and E. J. M. Hensen, Theory of surface chemistry and reactivity of reducible oxides, Catalysis Today **244**, 63 (2015).

[58] Th. Pillo, R. Zimmermann, P. Steiner, and S. Hüfner, The electronic structure of PdO found by photoemission (UPS and XPS) and inverse photoemission (BIS), J. Phys.: Condens. Matter **9**, 3987 (1997).

[59] V. Val. Sobolev, D. O. Mordas, and V. V. Sobolev, Optical properties and electronic structure of PdO, Inorg. Mater. **40**, 166 (2004).

[60] J. A. Kurzman, Mao-Sheng Miao, and R. Seshadri, Hybrid functional electronic structure of $PbPdO_2$, a small-gap semiconductor, J. Phys.: Condens. Matter **23**, 465501 (2011).

[61] K.-T. Park, D. L. Novikov, V. A. Gubanov, and A. J. Freeman, Electronic structure of noble-metal monoxides: PdO, PtO, and AgO, Phys. Rev. B **49**, 4425 (1994).

[62] M. K. Bruska, I. Czekaj, B. Delley, J. Mantzaras, and A. Wokaun, Electronic structure and oxygen vacancies in PdO and ZnO: Validation of DFT models, Phys. Chem. Chem. Phys. **13**, 15947 (2011).

[63] Y. Holl, G. Krill, A. Amamou, P. Légaré, L. Hilaire, and G. Maire, Electronic structure of PdO studied by photoemission (XPS, UPS), Solid State Commun. **32**, 1189 (1979).

[64] T. Uozumi, T. Okane, K. Yoshii, T. A. Sasaki, and A. Kotani, Theoretical and experimental study of resonant 3*d* x-ray photoemission and resonant l 3m 45m 45 auger transition of PdO, J. Phys. Soc. Jpn. **69**, 1226 (2000).

[65] C. W. Bauschlicher, Jr., C. J. Nelin, and P. S. Bagus, Transition metal oxides: CrO, MoO, NiO, PdO, AgO, J. Chem. Phys. **82**, 3265 (1985).

[66] E. B. Isaacs and C. Wolverton, Inverse band structure design via materials database screening: Application to square planar thermoelectrics, Chem. Mater. **30**, 1540 (2018).

[67] S. Ayukawa, M. Kato, T. Noji, and Y. Koike, Electrical properties of layered perovskite-type palladium oxides, Mater. Sci. Eng. B **148**, 65 (2008).

[68] S. Suzuki, K. Kawashima, W. Ito, S. Igarashi, M. Yoshikawa, and J. Akimitsu, Transport and magnetic properties of $Ln_{2-x}Ce_xPdO_4$ (Ln= Nd, Sm, and Eu) with the PdO_2 layer, JPS Conf. Proc. **3**, 017028 (2014).

[69] S. Shibasaki and I. Terasaki, Thermoelectric properties of layered Pd oxide R_2PdO_4 (R= La, Nd, Sm, and Gd), J. Phys. Soc. Jpn. **75**, 024705 (2006).

[70] H. Yamamoto, Y. Krockenberger, and M. Naito, Multi-source MBE with high-precision rate control system as a synthesis method *sui generis* for multi-cation metal oxides, J. Cryst. Growth **378**, 184 (2013).

[71] The growth rates appear to indicate that a substantial amount of Pd reevaporates as PdO from the film surface.

[72] I. Tanaka, N. Komai, and H. Kojima, Phase equilibrium in the NdCeCuO system, Physica C: Superconductivity **190**, 112 (1991).

[73] R. D. Shannon, Revised effective ionic radii and systematic studies of interatomic distances in halides and chalcogenides, Acta Crystallogr. Sect. A **32**, 751 (1976).

[74] F. Arrouy, C. Cros, and G. Demazeau, On the La_2CuO_4-Nd_2CuO_4 system: Influence of oxygen pressure on the phase diagram, oxygen stoichiometry and transport properties of the T/O and T′ type solid solutions, High Press. Res. **12**, 307 (1994).

[75] H. Wilhelm, C. Cros, F. Arrouy, and G. Demazeau, Pressure induced structural transition in the solid-solution $La_{2-x}Nd_xCuO_4$ for $x = 0.6$, 0.7, 1.2, and 1.5, J. Solid State Chem. **126**, 88 (1996).

[76] S. J. Schneider and R. S. Roth, Phase equilibria in systems involving rare earth oxides, part II, J. Res. Natl. Bur. Stand. A **64**, 317 (1960).

[77] J. A. Purton and N. L. Allan, Multi-million atom Monte Carlo simulation of oxide materials and solid solutions, Comput. Mater. Sci. **103**, 244 (2015).

[78] K. T. Jacob, K. T. Lwin, and Y. Waseda, Systematic trends in structural and thermodynamic properties of ternary oxides in the systems Ln-Pd-O (Ln = lanthanide element), Calphad **26**, 385 (2002).

[79] K. Kobayashi, Y. Tomita, and Y. Takagi, Electric and magnetic properties of $Nd_{2-x}Ce_xPdO_4$ with layered structure, Trans. Mater. Res. Soc. Jpn. **26**, 31 (2001).

[80] N. F. Mott and E. A. Davis, *Electronic Processes in Non-Crystalline Materials* (Clarendon, New York, 1979).

[81] M. C. Militello and S. J. Simko, Palladium oxide (PDO) by XPS, Surf. Sci. Spectra **3**, 395 (1994).

[82] M. Brun, A. Berthet, and J. C. Bertolini, XPS, AES and Auger parameter of Pd and PdO, J. Electron Spectrosc. Relat. Phenom. **104**, 55 (1999).

[83] NIST x-ray photoelectron spectroscopy database, 2012, https://srdata.nist.gov/xps/Default.aspx.

[84] D. A. Shirley, High-resolution x-ray photoemission spectrum of the valence bands of gold, Phys. Rev. B **5**, 4709 (1972).

[85] D. Zemlyanov, B. Klötzer, H. Gabasch, A. Smeltz, F. H. Ribeiro, S. Zafeiratos, D. Teschner, P. Schnörch, E. Vass, M. Hävecker, A. Knop-Gericke, and R. Schlögl, Kinetics of palladium oxidation in the mbar pressure range: Ambient pressure XPS study, Top. Catal. **56**, 885 (2013).

[86] G. Bayer and H. G. Wiedemann, Formation, dissociation and expansion behavior of platinum group metal oxides (PdO, RuO_2, IrO_2), Thermochim. Acta **11**, 79 (1975).

[87] C. A. Krier and R. I. Jaffee, Oxidation of the platinum-group metals, J. Less-Common Met. **5**, 411 (1963).

[88] J. H. Norman, H. Gene Staley, and Wayne E. Bell, Mass spectrometric Knudsen cell measurements of the vapor pressure of palladium and the partial pressure of palladium oxide, J. Phys. Chem. **69**, 1373 (1965).

[89] Note that the annealing process not only evacuates Pd but also oxygen ions and their loss results in a formally higher electron carrier concentration.

[90] L. K. Lamontagne, G. Laurita, M. Knight, H. Yusuf, J. Hu, R. Seshadri, and K. Page, The role of structural and compositional heterogeneities in the insulator-to-metal transition in hole-doped APd_3O_4 (A=Ca, Sr), Inorg. Chem. **56**, 5158 (2017).

[91] J. Maguire, R. Murray, R. C. Newman, R. B. Beall, and J. J. Harris, Mechanism of compensation in heavily silicon-doped gallium arsenide grown by molecular beam epitaxy, Appl. Phys. Lett. **50**, 516 (1987).

[92] N. E. Hussey, K. Takenaka, and H. Takagi, Universality of the Mott-Ioffe-Regel limit in metals, Philos. Mag. **84**, 2847 (2004).

[93] K. Luna, P. Giraldo-Gallo, T. Geballe, I. Fisher, and M. Beasley, Disorder Driven Metal-Insulator Transition in $BaPb_{1-x}Bi_xO_3$ and Inference of Disorder-Free Critical Temperature, Phys. Rev. Lett. **113**, 177004 (2014).

[94] K. Ueno, S. Nakamura, H. Shimotani, H. T. Yuan, N. Kimura, T. Nojima, H. Aoki, Y. Iwasa, and M. Kawasaki, Discovery of superconductivity in $KTaO_3$ by electrostatic carrier doping, Nat. Nanotech. **6**, 408 (2011).